

18. R. J. Thomas, R. Starr, C. J. Crannell, *Sol. Phys.* **95**, 323 (1985).
19. H. A. Garcia, *Sol. Phys.* **154**, 275 (1994).
20. R. Jenkins and J. DeVries, *Practical X-ray Spectrometry* (Springer-Verlag, New York, 1967).
21. P. Gorenstein, H. Gursky, G. Garmire, *Astrophys. J.* **153**, 885 (1968).
22. B. L. Henke, E. M. Gullikson, J. C. Davis, *At. Data Nucl. Data Tables* **54**, 181 (1993).
23. A. H. Compton and S. K. Allison, *X-rays in Theory and Experiment* (Van Nostrand, Princeton, NJ, 1935), appendix IV.
24. L. R. Nittler, P. E. Clark, T. J. McCoy, M. E. Murphy, J. I. Trombka, in *Asteroids, Comets, Meteors '99* (1999).
25. \_\_\_\_\_, *Lunar Planet. Sci. Conf. XXXI*, abstract 1711 (2000) [CD-ROM].
26. D. W. Mittlefehldt, T. J. McCoy, C. A. Goodrich, A. Kracher, in *Planetary Materials*, J. J. Papike, Ed. (Mineralogical Society of America, Washington, DC, 1998), pp. 41–195.
27. H. C. Urey and H. Craig, *Geochim. Cosmochim. Acta* **4**, 36 (1953).
28. T. J. McCoy *et al.*, *Icarus*, in press.
29. G. Kullerud, *Annu. Rep. Geophys. Lab.* **67**, 4055 (1963).
30. A. E. Rubin and S. Arnold, *Meteorit. Planet. Sci.* **35** (suppl.), A138 (2000).
31. T. P. McClanahan *et al.*, *Nucl. Instrum. Methods Phys. Res. A* **422**, 582 (1999).
32. We thank the NEAR project offices at Johns Hopkins University/Applied Physics Laboratory (JHU/APL) and NASA Headquarters. The NEAR mission is supported by

NASA Task 005 NASA contract NAS 5-97271, by NASA contract 624-03-03, and by the Planetary Instrument Definition and Development Program under NASA contract 344-96-30. The XGRS Team also recognizes the exemplary efforts of the NEAR Mission Operations Team and the NEAR Science Data Center at JHU/APL for enabling the collection of the data that have made this analysis possible. We thank the student support at Cornell University, the University of Arizona, and Goddard Space Flight Center. The contributions of P. Solomon are greatly appreciated. We would particularly like to acknowledge the late Isidore Adler, a pioneer in establishing x-ray remote sensing for planetary geochemical exploration and the late Jurgen Rahe, an unwavering supporter of the NEAR mission.

17 August 2000; accepted 28 August 2000

## The Kondo Effect in the Unitary Limit

W. G. van der Wiel,<sup>1\*</sup> S. De Franceschi,<sup>1</sup> T. Fujisawa,<sup>2</sup> J. M. Elzerman,<sup>1</sup> S. Tarucha,<sup>2,3</sup> L. P. Kouwenhoven<sup>1</sup>

We observe a strong Kondo effect in a semiconductor quantum dot when a small magnetic field is applied. The Coulomb blockade for electron tunneling is overcome completely by the Kondo effect, and the conductance reaches the unitary limit value. We compare the experimental Kondo temperature with the theoretical predictions for the spin- $1/2$  Anderson impurity model. Excellent agreement is found throughout the Kondo regime. Phase coherence is preserved when a Kondo quantum dot is included in one of the arms of an Aharonov-Bohm ring structure, and the phase behavior differs from previous results on a non-Kondo dot.

The Kondo theory explains the increased resistivity of a metal with magnetic impurities at low temperatures ( $I$ ). Predictions from 1988 indicate that quantum dots could also exhibit the Kondo effect ( $2-7$ ) as an increased conductance  $G$ , which can reach the unitary limit ( $G = 2e^2/h$ , where  $e$  is the electronic charge and  $h$  is Planck's constant) at low temperature. Recent experiments have confirmed the presence of the Kondo effect in quantum dots; however, the unitary limit was not reached ( $8-12$ ). We demonstrate the unitary limit Kondo effect in a semiconductor quantum dot. Our quantum dot is embedded in one of the arms of an Aharonov-Bohm (AB) ring, which enables us to show that electron transport through the many-body Kondo state is at least partly phase coherent.

The Kondo effect arises from the coupling between a localized electron spin and a sea of conduction electrons. The strength is characterized by the Kondo temperature  $T_K$  ( $13$ )

$$T_K = \frac{\sqrt{\Gamma U}}{2} e^{\pi\epsilon_0(e_0 + U)/\Gamma U} \quad (1)$$

$U$  is the on-site electron repulsion energy, or charging energy;  $\epsilon_0$  is the energy of the single-particle state; and  $\Gamma$  reflects its width, due to a finite lifetime from tunneling to the leads. In quantum dots, these parameters can be controlled experimentally, resulting in a "tunable Kondo effect" ( $8-12$ ).

Our device (Fig. 1A) consists of an AB ring defined in a two-dimensional electron gas (2DEG) ( $14$ ). The conductance of the ring without applying gate voltages is  $\sim 10e^2/h$ , implying that the current is carried by several modes in each arm. In our experiment, a quantum dot has only been formed in the lower arm. One gate in the upper arm is used to pinch off the upper arm. All measurements are performed in a dilution refrigerator with a base temperature of 15 mK, using a standard lock-in technique with an ac voltage excitation between source and drain contacts of  $3 \mu\text{V}$ .

The linear-response conductance  $G$  through the lower dot versus gate voltage  $V_{\text{gl}}$  and magnetic field  $B$  is shown in Fig. 1B. Here, the left and right parts of the lower arm serve as leads to the dot. In Fig. 1C, two  $G(V_{\text{gl}})$  curves are extracted from Fig. 1B for  $B = 0$  and  $0.4$  T. At  $B = 0$ , regular Coulomb oscillations are observed with low valley conductance. In some magnetic field ranges, however, the valley con-

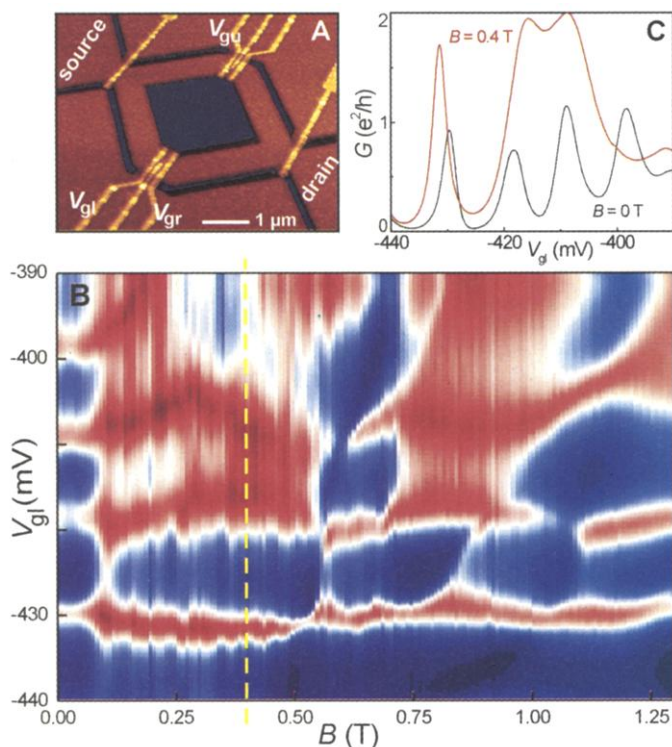
ductance increases considerably and can even reach  $2e^2/h$  (for instance, for  $B = 0.4$  T). Figure 1B is discussed in more detail below, but first, we focus on the large conductance values observed at  $B = 0.4$  T.

Figure 2A shows Coulomb oscillations for different temperatures. At the base temperature, the valleys around  $V_{\text{gl}} = -413$  and  $-372$  mV reach the maximum possible conductance value of  $2e^2/h$ . In fact, the valleys tend to disappear. When the temperature is increased, two separate Coulomb peaks develop with growing peak spacing. The conductance in the center of the valley has a logarithmic  $T$  dependence with a saturation at  $2e^2/h$  for low  $T$ , which is not due to electronic noise (Fig. 2A, right inset). The adjacent Coulomb valleys show an opposite  $T$  dependence. This even-odd asymmetry indicates an unpaired spin in a valley with an odd electron number, where we observe the Kondo anomaly, and a spin singlet for an even electron number ( $8, 9$ ). Figure 2B shows the differential conductance for different  $T$  values in the middle of the Kondo plateau at  $2e^2/h$ . The pronounced peak around  $V_{\text{SD}} = 0$  reflects the Kondo resonance at the Fermi energy ( $V_{\text{SD}}$  is the dc bias voltage between source and drain contacts). The peak height has the same  $T$  dependence as shown in Fig. 2A, right inset. The width of the peak increases linearly with temperature (Fig. 2B, inset).

These measurements are taken after optimizing the two barrier gate voltages,  $V_{\text{gl}}$  and  $V_{\text{gr}}$ , to obtain nearly equal tunnel barriers. However, sweeping  $V_{\text{gl}}$ , as in Fig. 2A, changes the left barrier much more effectively than the right tunnel barrier, and hence the barriers cannot be symmetric over the whole  $V_{\text{gl}}$  range. For a quantitative comparison to theory, we therefore optimize  $V_{\text{gr}}$  by fixing it at a value chosen such that, upon sweeping  $V_{\text{gl}}$ , we obtain a flat plateau close to  $2e^2/h$  (Fig. 3A) ( $15$ ). The two discernable Coulomb oscillations at higher temperatures have completely merged together at low temperature. This unitary limit was predicted ( $3, 4$ ) but not observed before. The unitary limit implies that the transmission probability through the quantum dot is equal to one. This is a remarkable phenomenon because the quantum dot contains two tunnel barriers, each with a

<sup>1</sup>Department of Applied Physics, Delft Institute for Microelectronics and Submicronotechnology, and ERATO Mesoscopic Correlation Project, Delft University of Technology, Post Office Box 5046, 2600 GA Delft, Netherlands. <sup>2</sup>NTT Basic Research Laboratories, Atsugi-shi, Kanagawa 243-0198, Japan. <sup>3</sup>ERATO Mesoscopic Correlation Project, University of Tokyo, Bunkyo-ku, Tokyo 113-0033, Japan.

\*To whom correspondence should be addressed. E-mail: wilfred@qt.tn.tudelft.nl



**Fig. 1 (left).** (A) Atomic force microscope image of the device. An AB ring is defined in a 2DEG by dry etching of the dark regions (depth is  $\sim 75$  nm). The 2DEG with electron density  $n_s = 2.6 \times 10^{15} \text{ m}^{-2}$  is situated 100 nm below the surface of an AlGaAs/GaAs heterostructure. In both arms of the ring (lithographic width,  $0.5 \mu\text{m}$ ; inner perimeter,  $6.6 \mu\text{m}$ ), a quantum dot can be defined by applying negative voltages to gate electrodes. The gates at the entry and exit of the ring are not used. A quantum dot of size  $\sim 200$  nm by  $200$  nm, containing  $\sim 100$  electrons, is formed in the lower arm using gate voltages  $V_{gl}$  and  $V_{gr}$  (the central plunger gate was not working). The average energy spacing between single-particle states is  $\sim 100 \mu\text{eV}$ . The conductance of the upper arm, set by  $V_{gu}$ , is kept at zero, except for AB measurements. (B) Color plot of the conductance  $G$  as function of  $V_{gl}$  and  $B$  for  $V_{gr} = -448$  mV and  $T = 15$  mK. The upper arm of the AB ring is pinched off by  $V_{gu} = -1.0$  V. Red and blue correspond to high and low conductance, respectively. (C) Two selected traces  $G(V_{gl})$  for  $B = 0$  and  $0.4$  T. The Coulomb oscillations at  $B = 0$  correspond to the oscillating color in (B). For some ranges of  $B$ , the valley conductance increases considerably, reaching values close to  $2e^2/h$ , i.e., the unitary limit [e.g., along the yellow dashed line at  $0.4$  T in (B)].

**Fig. 2 (right).** (A) Coulomb oscillations in  $G$  versus  $V_{gl}$  at  $B = 0.4$  T for different temperatures.  $T$  ranges from  $15$  mK (thick black trace) up to  $800$  mK (thick red trace).  $V_{gr}$  is fixed at  $-448$  mV. The red line in the right inset highlights the logarithmic  $T$  dependence between  $\sim 90$  and  $\sim 500$  mK for  $V_{gl} = -413$  mV. The left inset explains the variables used in the text with  $\Gamma = \Gamma_L + \Gamma_R$ .  $\epsilon_0$  is negative and measured from the Fermi level in the leads at equilibrium. (B) Differential conductance  $dI/dV_{SD}$  versus dc bias voltage between source and drain contacts  $V_{SD}$  for  $T$  ranging from  $15$  mK (thick black trace) up to  $900$  mK (thick red trace), at  $V_{gl} = -413$  mV and  $B = 0.4$  T. The inset shows that the width of the zero-bias peak, measured from the FWHM, increases linearly with  $T$ . The red line indicates a slope of  $1.7 k_B/e$ . At  $15$  mK, the FWHM =  $64 \mu\text{V}$ , and it starts to saturate around  $300$  mK.

transmission probability of much less than one. In addition, the on-site Coulomb energy  $U$  tends to block the state with an extra electron on the dot. Although  $U$  is an order of magnitude larger than the characteristic energy scale  $k_B T_K$  ( $k_B$  is the Boltzmann constant), the Kondo effect completely determines electron tunneling at low energies (i.e., low  $T$  and  $V_{SD}$ ). In the absence of the Kondo effect (e.g., for electron number  $N = \text{even}$ ), the system consists of two separated Fermi seas. In contrast, for  $N = \text{odd}$ , the screening of the local spin creates a single, extended many-body system with a single, well-defined Fermi surface extending throughout the whole system. The quasiparticles at this Fermi surface no longer experience the repulsive barrier potentials nor the on-site Coulomb repulsion. Because the local spin for  $N = \text{odd}$  is completely screened and because the dot has zero spin for

$N = \text{even}$ , the whole system of leads and dot is in a singlet state over a wide gate voltage range (between  $-430$  and  $-350$  mV in Fig. 2A), although the nature of the ground state in the even and odd valleys is very different.

For a quantitative analysis, we rewrite Eq. 1 as  $\ln(T_K) = \pi\epsilon_0(\epsilon_0 + U)/\Gamma U + \text{constant}$ , indicating a quadratic dependence for  $\ln(T_K)$  on gate voltage  $V_{gl}$  (16). Following the work in (17), we fit  $G$  versus  $T$  for different gate voltages (Fig. 3C) to the empirical function

$$G(T) = G_0 \left( \frac{T_K^2}{T^2 + T_K^2} \right)^s \quad (2)$$

with  $T_K' = T_K/(2^{1/s} - 1)^{1/2}$ , where the fit parameter  $s \approx 0.2$  for a spin- $1/2$  system (17, 18). Figure 3B shows the obtained Kondo temperatures  $T_K$  versus  $V_{gl}$ . The red parabola

demonstrates that the obtained values for  $T_K$  are in excellent agreement with Eq. 1 (19).

The Kondo temperature, as derived above, is obtained from the linear response conductance. In earlier works (8–12), estimates for  $T_K$  were obtained from measurements of  $dI/dV_{SD}$  versus  $V_{SD}$  ( $I$  is the current between source and drain). In that case, the full width at half maximum (FWHM) was set equal to  $k_B T_K/e$ . However, applying a finite  $V_{SD}$  introduces dephasing even at  $T = 0$  (6, 20). To compare these two methods, we also plot FWHM/ $k_B$  measured for different gate voltages at the base temperature (Fig. 3B). Also, now we find a parabolic dependence, but the values are larger than  $T_K$  obtained from linear-response measurements. The difference may indicate the amount of dephasing due to a nonzero  $V_{SD}$ .

The normalized conductance,  $G/(2e^2/h)$ , is

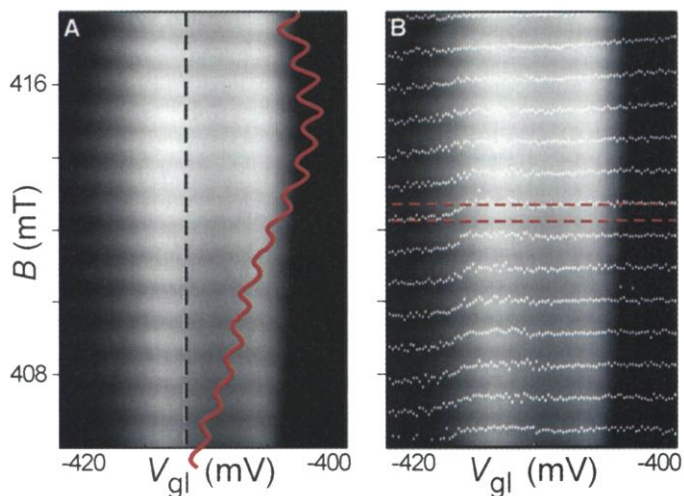
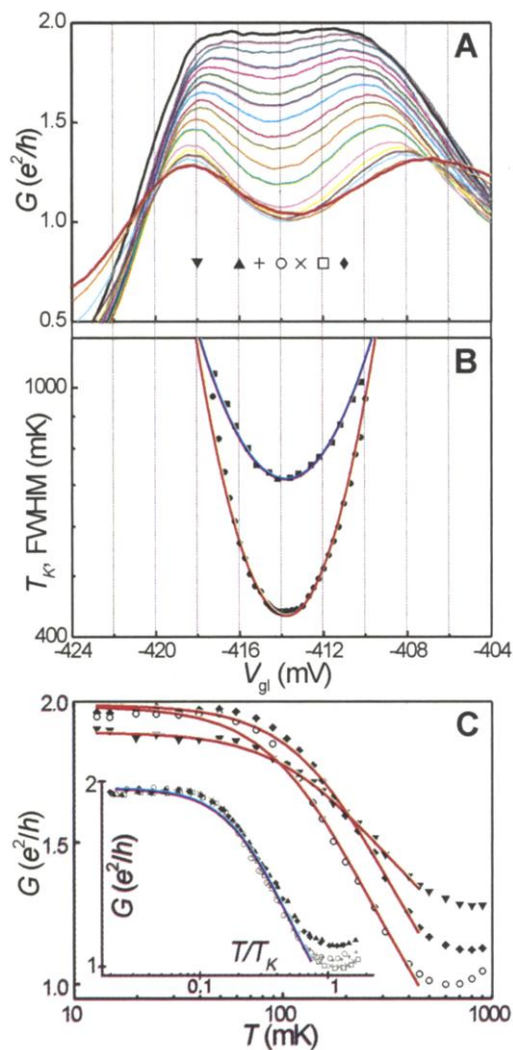


**Fig. 3 (left).** Quantitative analysis in the case of optimized symmetric tunnel barriers. **(A)**  $G(V_{gi})$  for  $T$  ranging from 15 mK (thick black trace) up to 900 mK (thick red trace) and  $V_g = -448$  mV and  $B = 0.4$  T. **(B)**  $T_K$  versus  $V_{gi}$  ( $\bullet$ ) as obtained from many fits as in **(C)**. In addition, we plot the peak width (FWHM/ $k_B$ ) versus  $V_{gi}$  ( $\blacksquare$ ) as deduced from  $dI/dV_{SD}(V_{SD})$  measurements at the base temperature (see, e.g., black trace in Fig. 2B). Both data sets are fitted to Eq. 1, resulting in the red and blue parabolas. **(C)**  $G(T)$  at fixed gate voltage as extracted from **(A)** for  $V_{gi} = -411$  ( $\blacklozenge$ ),  $-414$  ( $\circ$ ), and  $-418$  ( $\blacktriangledown$ ) mV [labels are also indicated in **(A)**]. The red curves are fits to Eq. 2. The inset shows that  $G$  versus normalized temperature  $T/T_K$  scales to a single curve for different gate voltages  $V_{gi} = -411$  ( $\blacklozenge$ ),  $-412$  ( $\square$ ),  $-413$  ( $\times$ ),  $-414$  ( $\circ$ ),  $-415$  ( $+$ ), and  $-416$  ( $\blacktriangle$ ) mV. The blue curve is a fit to Eq. 2 with fixed  $T_K = 1$  and  $G_0 = 2e^2/h$ ;  $s = 0.29$  is the only fit parameter. **Fig. 4 (right).** AB oscillations in the conductance through the ring containing the unitary Kondo quantum dot. In this measurement, the conductance through the upper arm is set close to  $2e^2/h$  in order to have approximately equal transmissions through both arms. **(A)** Gray-scale plot of the conductance  $G$  as a function of  $V_{gi}$  and magnetic field  $B$  at 15 mK. Light and dark areas corresponds to high and low conductance, respectively. AB oscillations are observed over the whole gate voltage range. The red curve highlights the AB oscillations in the middle of the Kondo plateau ( $V_{gi} = -412$  mV). The period of 0.87 mT corresponds well to a flux quantum  $h/e$  through the area enclosed by the ring. The modulation is 2 to 3% of the total conductance through the ring. **(B)** Same gray-scale plot as in **(A)**, with the AB conductance maxima indicated by white diamond symbols. A  $\pi$  phase flip is observed when stepping through the left

Coulomb peak (e.g., along the red dashed lines). No phase change is observed in the Kondo valley or at the right Coulomb peak.

expected to be a universal function of the normalized temperature,  $T/T_K$ , independent of the other energy scales ( $U$ ,  $\epsilon_0$ , and  $\Gamma$ ). Over a range of  $\Delta\epsilon_0 = 225$   $\mu$ eV corresponding to 2.6 K, which is several times larger than  $T_K$ , this expected one-parameter scaling is observed in Fig. 3C, inset.

We now return to the importance of the applied magnetic field. Near  $B = 0$ , we observe regular Coulomb oscillations (Fig. 1B). Here, we find that the Kondo effect typically changes the valley conductance by only  $\sim 20\%$  (9). In Fig. 1B, a big change occurs at  $B \sim 0.1$  T, reflecting the onset of a different transport regime, an observation that seems common for half-open quantum dots (21, 22). The magnetic field scale corresponds to adding a flux quantum to the area of the dot, implying, for instance, that time-reversal symmetry is broken. At  $B = 0.4$  T, where we observe the unitary limit, the Zeeman spin splitting is much smaller than  $k_B T_K$ , and so it can safely be ignored. This magnetic field scale is also too small for the formation of Landau levels, which can introduce additional spin physics (22, 23).

Recent calculations (24) indicate a spin polarization near  $B = 0$  to enhanced values in line with earlier observations (25, 26). A small magnetic field reduces the spin values to  $1/2$  for  $N = \text{odd}$  and 0 for  $N = \text{even}$ . Because higher spin states generally lead to a lower Kondo temperature, the Kondo effect can become much stronger by applying a magnetic field (27). We think that this is the origin for the transition in transport regimes near  $B = 0.1$  T in Fig. 1B, although a thorough theoretical analysis would be desirable.

So far, the upper arm of the ring was pinched off. To study how electron interference is affected by a Kondo quantum dot in the lower arm, we adjust the upper arm conductance to  $\sim 2e^2/h$ . In the gray-scale plot of Fig. 4A, clear AB oscillations around  $B = 0.4$  T are visible in the Kondo valley and in the neighboring valleys. The period agrees well with a flux quantum  $h/e$ , applied through the area enclosed by the ring. The AB oscillations demonstrate that at least part of the tunnel processes through the Kondo quantum dot is phase coherent. Our two-terminal geometry only allows

phase changes by multiples of  $\pi$ , because of symmetry reasons (28). We observe a  $\pi$  phase flip at the left Coulomb peak, but no phase change is observed in the Kondo valley or at the right Coulomb peak (Fig. 4B). This behavior is different from the phase evolution described in (14). A further study in a four-terminal geometry should allow us to determine arbitrary phase shifts in the transmission through a Kondo dot, as proposed in (29).

#### References and Notes

1. J. Kondo, *Prog. Theor. Phys.* **32**, 37 (1964).
2. L. I. Glazman and M. E. Raikh, *JETP Lett.* **47**, 452 (1988).
3. T. K. Ng and P. A. Lee, *Phys. Rev. Lett.* **61**, 1768 (1988).
4. A. Kawabata, *J. Phys. Soc. Jpn.* **60**, 3222 (1991).
5. Y. Meir, N. S. Wingreen, P. A. Lee, *Phys. Rev. Lett.* **70**, 2601 (1993).
6. N. S. Wingreen and Y. Meir, *Phys. Rev. B* **49**, 11040 (1994).
7. W. Izumida, O. Sakai, Y. Shimizu, *J. Phys. Soc. Jpn.* **67**, 2444 (1998).
8. D. Goldhaber-Gordon et al., *Nature* **391**, 156 (1998).
9. S. M. Cronenwett, T. H. Oosterkamp, L. P. Kouwenhoven, *Science* **281**, 540 (1998).
10. J. Schmid, J. Weis, K. Eberl, K. von Klitzing, *Physica B* **256–258**, 182 (1998).

11. F. Simmel, R. H. Blick, J. P. Kotthaus, W. Wegscheider, M. Bichler, *Phys. Rev. Lett.* **83**, 804 (1999).  
 12. S. Sasaki *et al.*, *Nature* **405**, 764 (2000).  
 13. F. D. M. Haldane, *Phys. Rev. Lett.* **40**, 416 (1978).  
 14. A. Yacoby, M. Heiblum, D. Mahalu, H. Shtrikman, *Phys. Rev. Lett.* **74**, 4047 (1995).  
 15. The Kondo region around  $-372$  mV does not develop a plateau at  $2e^2/h$ . In this gate voltage regime, the tunnel coupling can be rather large so that charge fluctuations become important. This regime has been described by L. I. Glazman, F. W. J. Hekking, and A. I. Larkin [*Phys. Rev. Lett.* **83**, 1830 (1999)], who predict a similar rounded-off Kondo region.  
 16.  $e_0 = \alpha V_{gl} + \text{constant}$ , with  $\alpha = C_{gl}/C_{\Sigma} = 45 \mu\text{eV/mV}$ . Here,  $C_{gl}$  is the capacitance of the left gate electrode, and  $C_{\Sigma}$  is the total capacitance of the dot. Using this  $\alpha$  factor and the  $T$  dependence of  $G$ , we obtain  $U = 500 \mu\text{eV}$  and  $\Gamma = 240 \mu\text{eV}$ .  
 17. D. Goldhaber-Gordon *et al.*, *Phys. Rev. Lett.* **81**, 5225 (1998).  
 18. Equation 2 is an empirical fitting function to numerical renormalization group calculations reported in

work by T. A. Costi, A. C. Hewson, and V. Zlatic [*J. Phys. Condens. Matter* **6**, 2519 (1994)].  
 19. From these fits, we obtain  $\Gamma = 231 \pm 12 \mu\text{eV}$  by taking  $U = 500 \mu\text{eV}$ . Because  $\Gamma \gg k_B T_K$ , we conclude that the low-energy properties are set by  $T_K$ , which is required for Eq. 1, and that the dot is in the Kondo regime and not in the mixed-valence regime.  
 20. A. Kaminski, Yu. V. Nazarov, L. I. Glazman, e-Print available at <http://xxx.lanl.gov/abs/cond-mat/0003353>.  
 21. S. M. Maurer, S. R. Patel, C. M. Marcus, C. I. Duruöz, J. S. Harris Jr., *Phys. Rev. Lett.* **83**, 1403 (1999).  
 22. J. Schmid, J. Weis, K. Eberl, K. von Klitzing, *Phys. Rev. Lett.* **84**, 5824 (2000).  
 23. The theory developed in work by C. Tejedor and L. Martin-Moreno (e-Print available at <http://xxx.lanl.gov/abs/cond-mat/0003261>) to describe the experimental results in (22) requires the formation of Landau levels; therefore, it cannot describe our present results.  
 24. M. Stopa, unpublished data. The enhanced values for the spin polarization can sometimes reoccur at higher magnetic fields.

25. S. Tarucha, D. G. Austing, T. Honda, R. J. van der Hage, L. P. Kouwenhoven, *Phys. Rev. Lett.* **77**, 3613 (1996).  
 26. D. R. Stewart, D. Sprinzak, C. M. Marcus, C. I. Duruöz, J. S. Harris Jr., *Science* **278**, 1784 (1997).  
 27. M. Stopa, W. Izumida, M. Eto, private communication.  
 28. M. Büttiker, *Phys. Rev. Lett.* **57**, 176 (1986).  
 29. U. Gerland, J. von Delft, T. Costi, Y. Oreg, *Phys. Rev. Lett.* **84**, 3710 (2000).  
 30. We thank E. Huizeling, S. Sasaki, D. Goldhaber-Gordon, Y. Meir, M. Eto, L. Glazman, Yu. Nazarov, and R. Schouten for their help. We acknowledge financial support from the Specially Promoted Research, Grant-in-Aid for Scientific Research; the Ministry of Education, Science, and Culture in Japan; the Dutch Organization for Fundamental Research on Matter; the New Energy and Industrial Technology Development Organization Joint Research Program (NTDP-98); and the European Union through a Training and Mobility of Researchers Programme network.

8 June 2000; accepted 7 August 2000

# Graphical Evolution of the Arnold Web: From Order to Chaos

Claude Froeschlé, Massimiliano Guzzo,\* Elena Lega

We represent graphically the evolution of the set of resonances of a quasi-integrable dynamical system, the so-called Arnold web, whose structure is crucial for the stability properties of the system. The basis of our representation is the use of an original numerical method, whose definition is directly related to the dynamics of orbits, and the careful choice of a model system. We also show the transition from the Nekhoroshev stability regime to the Chirikov diffusive one, which is a generic nontrivial phenomenon occurring in many physical processes, such as slow chaotic transport in the asteroid belt and beam-beam interaction.

The long-term behavior of a mechanical system is in general unpredictable. In the frame-work of Hamiltonian systems, an exception is systems that are integrable in the sense of Liouville-Arnold. In these systems, the phase space is completely filled with invariant tori, and on each invariant torus all motions are quasi-periodic with the same frequencies  $\omega_1, \dots, \omega_n$ , where  $n$  is the number of degrees of freedom. Although Liouville-Arnold's integrability is a rare property, many mechanical systems of great interest are integrable, such as the Euler-Poinsot rigid body, the two-body problem, and the Birkhoff normal forms around elliptic equilibria truncated at suitable order.

Many interesting problems of physics, such as the stability of planets and asteroids, of planetary spin-axis, and of the

beam-beam interaction, among others, can be represented as small perturbations of integrable systems. In general, a small perturbation breaks the integrability of the system. Consequently, the behavior of the so-

lutions can become complex and unpredictable to such an extent that it is generically called chaotic. Small perturbations of integrable systems transform them into quasi-integrable systems, and their study is the subject of Hamiltonian perturbation theory. One of the most celebrated results of Hamiltonian perturbation theory is the KAM theorem (1-3), which applies if the perturbation is smooth (4) and suitably small (5) and if the integrable approximation of the system satisfies a nondegeneracy property (1, 3, 6-9). The KAM theorem establishes that for the majority of initial conditions, which we call the regularity set, the features of the motions of the system are essentially those of the integrable approximation: In the regularity set, motions occur on invariant tori, and on the same torus all motions are quasi-periodic with the same frequencies. More precisely, the KAM theorem proves that for any invariant torus of the original system with nonresonant frequencies [more precisely, Diophantine (10)], there exists an invariant torus in the regularity

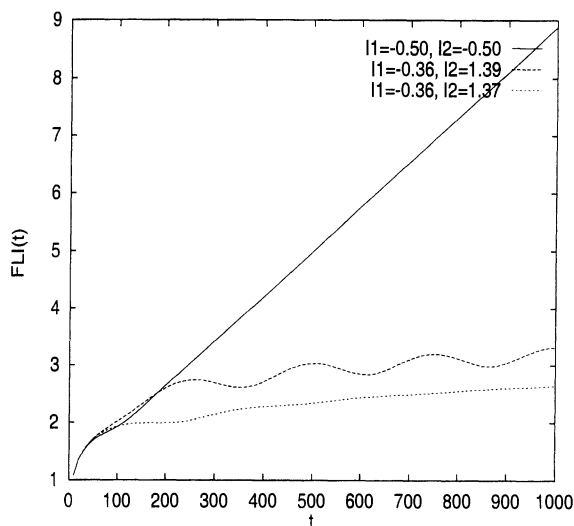


Fig. 1. Variation of the FLI for  $\epsilon = 0.01$  as a function of the integration time for a chaotic orbit (continuous line), a nonresonant one (dashed line), and a resonant one (dotted line). The three kinds of orbits are clearly distinguished already for  $t = 300$ .

Observatoire de Nice, Boulevard de l'Observatoire, Boîte Postale 4229, 06304 Nice Cedex 4, France.

\*Present address: Dipartimento di Matematica Pura ed Applicata, Università degli Studi di Padova, via Belzoni 7, 35131 Padova, Italy.